Materials Advances

ROYAL SOCIETY OF CHEMISTRY

PAPER

View Article Online
View Journal | View Issue





Cite this: *Mater. Adv.*, 2026, 7, 1790

# Construction of p-$ZnBi_2O_4$/n-BiOBr heterojunctions for efficient visible-light photocatalytic degradation of dyes

L. Mllaoiy, *[ab] B. Bakiz,*[a] A. Bouddouch,[c] S. Villain,[b] A. Taoufyq,[a] F. Guinneton,[b] J.-R. Gavarri[b] and A. Benlhachemi[a]

Received 12th August 2025,
Accepted 19th December 2025

DOI: 10.1039/d5ma00892a

rsc.li/materials-advances

A composite series, $(1-x)ZnBi_2O_4/x$-BiOBr, was synthesized using a two-step hydrothermal method. The $x$ = 0.7 composite demonstrated 100% removal of RhB in 10 minutes ($k$ = 0.2317 $min^{-1}$) under visible light, ~74 times higher than that of $ZnBi_2O_4$ ($k$ = 0.0031 $min^{-1}$). For Orange G, $x$ = 0.7 yielded 100% removal in 30 min with $k$ = 0.1053 $min^{-1}$, ~14 times greater than that of $ZnBi_2O_4$. The improved activity correlates with high $S_{BET}$ (21.8 $m^2$ $g^{-1}$) and good interfacial charge separation. Band-edge estimates and scavenger tests suggested a type-II-like band alignment. Moreover, the $x$ = 0.7 composite retained ≥81% of activity over 5 cycles.

## 1. Introduction

The escalating discharge of pollutants, resulting from rapid industrialization, into water bodies has emerged as a critical global environmental concern. Among these pollutants, organic dyes, widely employed in various industries including textiles, printing, and plastics, represent a particularly concerning class due to their persistence, potential toxicity, and aesthetic impact on water systems.[1,2] Conventional wastewater treatment techniques are frequently insufficient for the effective removal of these dyes, highlighting the need to explore more advanced treatment approaches.[3] Photocatalysis, a promising technology for environmental remediation, offers an efficient and sustainable approach to degrade organic pollutants, addressing a critical need in maintaining ecological balance and human health.[4]

Photocatalysis, an advanced oxidation process, harnesses the power of semiconductor materials to facilitate chemical reactions upon light irradiation.[5–7] Specifically, when a semiconductor photocatalyst is exposed to light with energy greater than its intrinsic band gap, electrons are excited from the valence band to the conduction band, thereby generating electron–hole pairs.[8–11] These photogenerated charge carriers can then migrate to the surface of the photocatalyst, where they initiate a series of redox reactions with adsorbed molecules, leading to the degradation of organic pollutants. Moreover, this process ultimately mineralizes organic contaminants into harmless substances such as carbon dioxide and water, providing a sustainable solution for water purification.[12–14] The efficiency of a photocatalytic process hinges on several key factors, including the light absorption characteristics, charge carrier separation and migration, and surface reactivity of the photocatalyst.[15]

Despite its potential, conventional photocatalysts like titanium dioxide $TiO_2$ suffer from limitations such as a wide band gap, restricting their activity to the ultraviolet region, which accounts for only a small fraction of the solar spectrum.[16–19] Furthermore, the fast recombination rate of photogenerated electron–hole pairs in these materials reduces their quantum efficiency, limiting their overall photocatalytic performance. To overcome these limitations, researchers have explored various strategies, including doping, surface modification, and the development of composite photocatalytic systems.[20]

The $ZnBi_2O_4$ semiconductor is characterized by its suitable band gap and excellent chemical stability, making it a promising component for photocatalytic applications.[21] Similarly, bismuth oxobromide has garnered considerable attention as a photocatalytic material due to its unique layered structure, high surface area, and excellent visible light absorption properties.[2] The combination of these two materials into type II heterostructures is expected to synergistically enhance their individual advantages, leading to improved photocatalytic performance.[22]

While several bismuth-based heterojunctions have been well documented in the literature, including $BiVO_4$,[23] $Bi_2O_3$,[24] and

[a] Materials and Environment Laboratory (LME), Faculty of Science, Ibn Zohr University, P.O. Box 8106, Cité Dakhla, Agadir, Morocco. E-mail: lhossain.mllaoiy@edu.uiz.ac.ma, bakizlahcen@gmail.com
[b] University of Toulon, University of Aix Marseille, CNRS 7334, IM2NP, BP 20132, La Garde Cedex, France
[c] Laboratory of Physical-Chemistry of Materials (LPCM), Department of Chemistry, Faculty of Sciences, Chouaïb Doukkali University, El Jadida, Morocco

BiOBr-based systems, the coupling of $ZnBi_2O_4$ and BiOBr has not been explored to the same degree and offers an interesting opportunity. The band-edge positions of $ZnBi_2O_4$ and BiOBr suggest a staggered Type-II heterojunction, which should facilitate better spatial separation of charge carriers compared to other Bi-based composites. However, a comprehensive study that explores how varying the molar ratio of these two elements ($ZnBi_2O_4$ *vs.* BiOBr) contributes to structural properties, surface area, and photocatalytic performance has not been conducted. This is the clear gap in the literature for optimization, given that the ratio of these components is likely the most important variable for modifying the heterojunction space charge layer and the photocatalytic efficiency.

## 2. Synthesis of the $ZnBi_2O_4$/BiOBr composite

This section details the procedure of synthesizing $ZnBi_2O_4$/BiOBr composite photocatalysts. For the pure samples, the synthesized method is detailed in the SI.

To synthesize the composite system $\{(1-x)ZnBi_2O_4/(x)BiOBr\}$ with $0 < x < 1$, we used the same synthesis method as for the BiOBr phase, by adding $ZnBi_2O_4$ as a solid precursor. In the first step, different amounts of $Bi(NO_3)_3{-}5H_2O$ were dissolved in 30 ml of distilled water to obtain solution A. In the second step, 0.3 g of $ZnBi_2O_4$ powder was mixed with solution A and stirred for 30 minutes. The corresponding quantity of KBr was dissolved in 10 ml of distilled water to obtain solution B which was then transferred to solution A (A + B = $ZnBi_2O_4$ + BiOBr), as Fig. 1 shows. Finally, the mixture was placed in a Teflon-lined autoclave and kept in an oven at 160 °C for 16 h. The resulting product was collected, washed with water and dried. A full series of molar fractions was synthesized to screen for the optimal heterojunction ratio. The compositions $x$ = 0.1, 0.3, 0.5, 0.7, and 0.9 are presented in detail to illustrate the evolution of photocatalytic activity, which was found to peak at $x$ = 0.7.

## 3. Characterization

Structural characterization of the synthesized samples was carried out using X-ray diffraction (XRD) with a Bruker D8 Advance Twin diffractometer, using a Cu Kα radiation source ($\lambda$ = 1.540–1.544 Å). To confirm the crystal phases of BiOBr and $ZnBi_2O_4$, Rietveld refinement analysis was employed. Raman spectroscopy was performed using a Horiba Jobin-Yvon HR800 LabRam spectrometer, equipped with a 633 nm laser, while maintaining low laser intensity to minimize thermal effects. Raman measurements were conducted in the spectral range of 50–800 $cm^{-1}$ to investigate the vibrational modes of the materials. Fourier-transform infrared (FTIR) spectra were obtained using a Nicolet iS5 spectrometer (Thermo Fisher Scientific, USA), covering the wavenumber range of 4000–400 $cm^{-1}$. The surface morphology and microstructural features were examined using a Zeiss Supra 40 VP scanning electron microscope (SEM). The elemental composition and distribution were analyzed using energy-dispersive X-ray spectroscopy (EDX) attached to the SEM, providing both qualitative and quantitative insights. Specific surface area ($S_{BET}$) measurements were conducted through nitrogen adsorption–desorption isotherms using a Micromeritics ASAP 2020. Optical properties were evaluated using a JASCO V-750 UV-vis diffuse reflectance spectrophotometer equipped with an integrating sphere, recording spectra from 200 to 800 nm, and the band gap energies were estimated using the Kubelka–Munk function. Photoluminescence (PL) emissions of the photocatalysts were also studied with a Horiba Jobin-Yvon HR800 LabRam spectrometer. Mott–Schottky plots were acquired using a platinum plate and saturated Ag/AgCl as the counter electrode and reference electrode, respectively, and 0.5 M $Na_2SO_4$ aqueous solution as the electrolyte. The working electrode was made by coating a slurry of 20 mg sample and 2 mL solution of distilled water/ethanol onto a 1 cm × 1 cm FTO glass electrode.

## 4. Photocatalytic test

The experiments of photodegradation were carried out using a visible light source (250 W ARC lamp; 20 mW $cm^{-2}$;

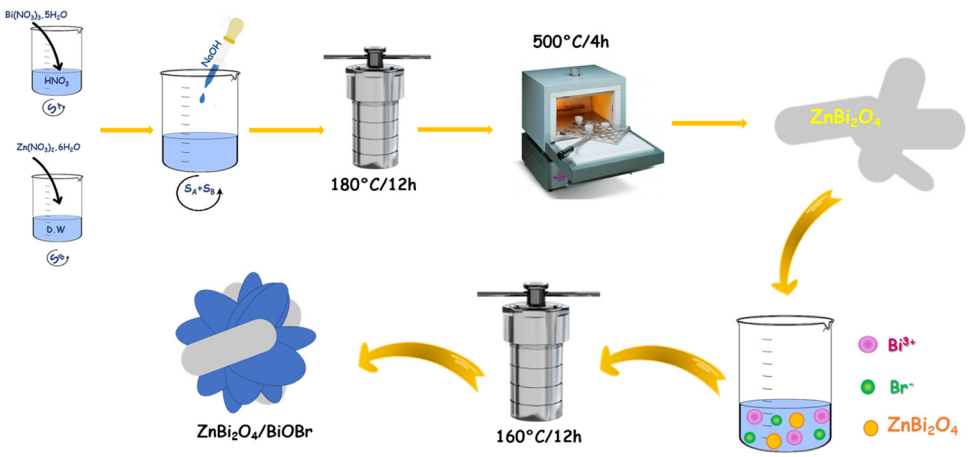


Fig. 1 Synthesis process of the $ZnBi_2O_4$/BiOBr composite.

420–800 nm) on pollutant molecules dissolved in distilled water. In a standard photocatalytic experiment, 0.05 g of the photocatalyst was dispersed in 50 mL of RhB and OG aqueous solution (10 mg $L^{-1}$). The suspension was stirred in the dark for 30 minutes to achieve adsorption–desorption equilibrium, followed by exposure to irradiation. The concentration $C_t$ in the solution was monitored for a period of time using ultraviolet-visible (UV-vis) absorption spectroscopy. Degradation efficiency ($D$(%)) was defined as follows (Eqn (1)):

$$D\ (\%) = \frac{C_0 - C_t}{C_0} \times 100 \quad (1)$$

Assuming a pseudo-first-order photocatalytic degradation mechanism, the apparent rate constant $K_{app}$ ($min^{-1}$) was determined using eqn (2):

$$\ln\left(\frac{C_t}{C_0}\right) = -K_{app}t \quad (2)$$

Here, $C_0$ represents the initial concentration of the pollutant, while $C_t$ denotes the concentration at a given time ($t$) in min.

## 5. Crystalline phase analysis

Fig. 2(a and b) displays the XRD patterns of BiOBr, $ZnBi_2O_4$, and $(1-x)ZnBi_2O_4/x$-BiOBr with $x$ ranging from 0 to 1. The main Bragg peaks of the BiOBr phase are located at $2\theta = 10.92^\circ$, $25.20^\circ$, $31.74^\circ$, $32.24^\circ$, $46.24^\circ$, and $57.18^\circ$ corresponding to the (0 0 1), (1 0 1), (1 0 2), (1 1 0), (2 0 0), and (2 1 2) planes, respectively, in agreement with the JCPDS card 153-9093. The primary XRD Bragg peaks of the $ZnBi_2O_4$ phase are located at $2\theta = 24.68^\circ$, $27.65^\circ$, $30.34^\circ$, and $32.84^\circ$, corresponding to the (0 2 2), (0 1 3), (2 2 2), and (1 2 3) planes, in agreement with the JCPDS card 153-6162. The XRD Bragg peaks of both BiOBr and $ZnBi_2O_4$ are present in the $ZnBi_2O_4$/BiOBr XRD patterns, with no additional peaks observed. Notably, the intensity of the diffraction peaks corresponding to the BiOBr phase in the composite increases with BiOBr rate $x$, which confirms the successful preparation of the composite photocatalyst.

The Rietveld refinement analysis of the as-synthesized $ZnBi_2O_4$ and BiOBr phases was performed to validate the structures and determine the cell parameters, using FullProf software.[25] The resulting observed and calculated XRD profile refinement patterns are depicted in Fig. 2(c and d). For the refinement process, the crystal structures of $ZnBi_2O_4$ and BiOBr

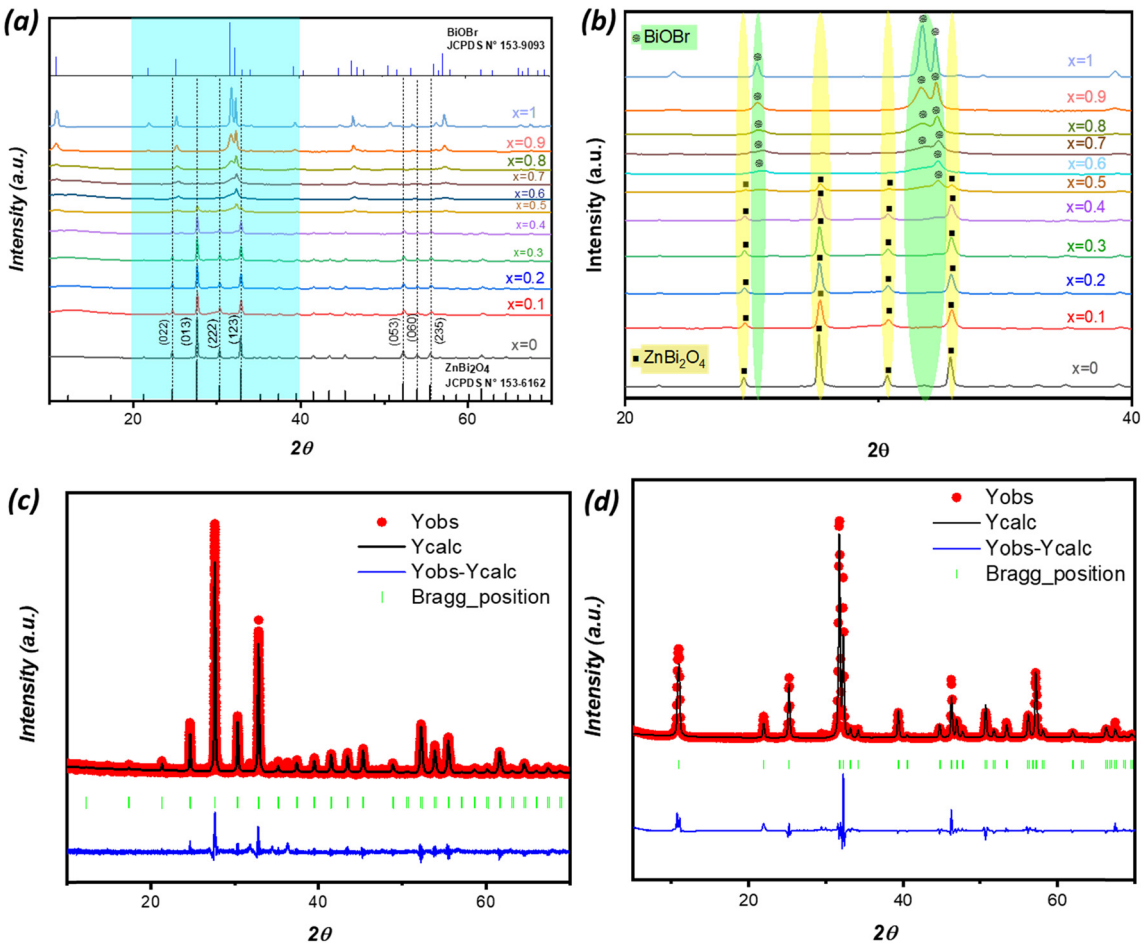


Fig. 2 (a) XRD patterns of the synthesized samples; (b) zoom out of the $2\theta$ value from 20 to 40; (c) the Rietveld refinement results for the cubic $ZnBi_2O_4$ phase and (d) the Rietveld refinement results for the tetragonal BiOBr phase.

Table 1 Crystal cell parameters and cell volumes of $ZnBi_2O_4$ and BiOBr samples from Rietveld analyses. Average crystallite sizes or coherence lengths from Bragg peak profile analyses

| BiOBr (tetragonal cell) | $ZnBi_2O_4$ (cubic cell) |
|---|---|
| Space group: *P*4/*nmm* | Space group: *I*23 |
| *a* (Å) = 3.9225 (3) | *a* (Å) = 10.2059 (5) |
| *c* (Å) = 8.1013 (7) | — |
| *V* (Å$^3$) = 124.671 (4) | *V* (Å$^3$) = 1063.079 (2) |
| $R_{wp}$ (%) = 22.7 | $R_{wp}$ (%) = 16.3 |
| $R_{exp}$ (%) = 13.9 | $R_{exp}$ (%) = 12.7 |
| $\chi^2$ = 2.66 | $\chi^2$ = 1.64 |
| *D*(XRD) = 150 ± 20 nm | *D*(XRD) = 40 ± 5 nm |

phases were assumed to be cubic, with space group *I*23, and tetragonal, with space group *P*4/*nmm*, respectively. The modelling of the XRD background used interpolation between a set of background points with adjustable heights, while the shape of the XRD peak was represented using the pseudo-Voigt function. Numerous parameters were adjusted during the refinement process, such as the scale factor, zero correction and background. Atom coordinates were fixed. Table 1 shows the structural parameters obtained after refinement, such as the network parameters and other relevant values. Finally, after several cycles of refinement, the main parameters obtained are cell parameters, cell volumes, and expected and reliability factors ($R_{exp}$, $R_{wp}$ and $\chi^2$). Rietveld refinement of the single-phase BiOBr sample (tetragonal, *P*4/*nmm*) provides *a* = 3.9225(3) Å, *c* = 8.1013(7) Å and *V* = 124.671(4) Å$^3$, with $R_{wp}/R_{exp}$ = 22.7/13.9% ($\chi^2$ = 2.66); the moderate mismatch in this *R*-factor suggests weak correlations like preferred orientation or microstrain one would typically expect for layered BiOBr. For the single-phase $ZnBi_2O_4$ sample (cubic, *I*23), we independently refine to *a* = 10.2059(5) Å and *V* = 1063.079(2) Å$^3$ with better agreement, $R_{wp}/R_{exp}$ = 16.3/12.7% ($\chi^2$ = 1.64). These $\chi^2$ low values, being close to 1, indicate a good match between the observed and calculated diffraction patterns and confirm the phase purity of the parent materials.

The crystallite size of the synthesized compounds was determined using Scherrer's equation (Eqn 3), based on the analysis of the full width at half maximum (FWHM) of the Bragg peaks, with corrections applied for instrumental broadening:

$$D = \frac{K \times \lambda}{\beta \times \cos\theta} \quad (3)$$

In this equation, $\beta$ (in radians) represents the corrected broadening of the Bragg peaks. The constant $K$ is the shape factor, taken as 0.9; $\lambda$ is the X-ray wavelength ($K\alpha_1$) equal to 1.540 Å; $D$ is the average crystallite size; and $\theta$ (in radians) is the diffraction angle.

## 6. Raman and FTIR analyses

Raman and Fourier transform infrared (FTIR) spectroscopies were employed to further elucidate the structural characteristics and phase evolution of the as-synthesized $(1-x)ZnBi_2O_4/x$-BiOBr composite materials as a function of BiOBr content ($x$). The Raman spectra (Fig. 3a) provide insight into the vibrational modes of the crystal lattices. For the pure $ZnBi_2O_4$ sample ($x$ = 0), characteristic vibrational modes of the Bi–O bonds are clearly observed at 160 cm$^{-1}$, and the peaks near 53 and 79 cm$^{-1}$ belong to the vibrational modes of Bi–Bi bonds,[26,27] with the peak near 531 cm$^{-1}$ corresponding to the Zn–O first order $E_1$ stretching mode.[28] As the BiOBr content '$x$' increases, the distinctive fingerprint of BiOBr becomes progressively prominent. Notably, the characteristic vibrational modes around 56 cm$^{-1}$, 90 cm$^{-1}$, 110 cm$^{-1}$, and 160 cm$^{-1}$ are attributed to the characteristic $A_{1g}$ and $E_g$ vibrational modes of tetragonal BiOBr, originating from the internal and external vibrations of the Bi–Br bonds and translational motions of $Bi^{3+}$ ions.[2] These observations confirm the successful incorporation and increasing proportion of the BiOBr phase within the composite system, while the original $ZnBi_2O_4$ peaks gradually diminish or are influenced by the growing BiOBr presence. Any subtle shifts or broadening of these vibrational bands might suggest interfacial interactions or strain effects within the heterojunctions formed between the two photocatalysts.

Complementary information was obtained from the FTIR spectra (Fig. 3b), which primarily highlight the absorption bands corresponding to various functional groups and metal–oxygen stretching vibrations. In the fingerprint region 400–1500 cm$^{-1}$, the FTIR spectrum of pure $ZnBi_2O_4$ ($x$ = 0) exhibits characteristic absorption bands at 548, 847, and 1396 cm$^{-1}$ attributed to the stretching vibrations of Zn–O, Bi–O–Bi, and Bi–O.[29,30] Upon increasing the BiOBr content, the evolution of this broad absorption feature confirms the formation of the composite, with new or altered bands reflecting the presence of BiOBr's Bi–O stretching modes at 506 cm$^{-1}$.[31] Furthermore, the broad band centered around 3400–3700 cm$^{-1}$ is attributed to the bending and stretching vibrations of adsorbed water molecules. The relative intensity of these bands can provide insights into the surface hydrophilicity and hydroxyl group concentration of the composite materials, which are relevant for photocatalytic activity. Overall, both Raman and FTIR spectroscopies collectively corroborate the successful formation of the $ZnBi_2O_4$/BiOBr composite materials and provide valuable insights into their evolving structural and bonding characteristics upon varying the BiOBr content. The small alterations and enlargement of the vibrational bands in the composite spectra relative to the pure phases suggest strong interfacial interactions among the $ZnBi_2O_4$ and BiOBr components in agreement with the successful fabrication of the heterojunctions.[32,33]

## 7. Scanning electron microscopy

In order to carry out a comparative morphological study between the different powder compositions developed from the $ZnBi_2O_4$/BiOBr system, a microstructural study was carried out by scanning electron microscopy (SEM) coupled with EDS microanalysis, which provides us with information on the

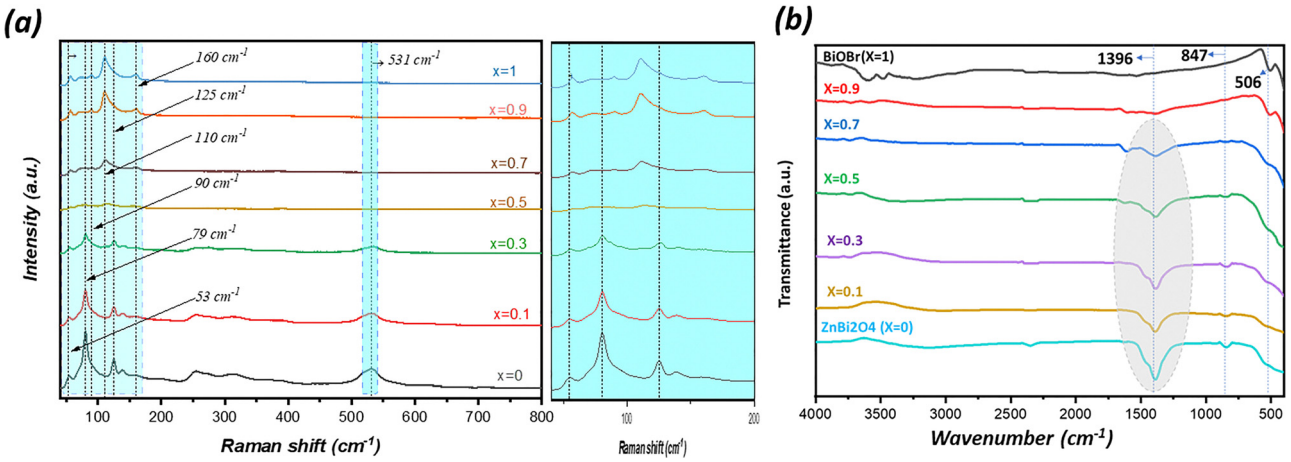


Fig. 3 (a) Raman spectra and (b) FTIR spectra of $(1 - x)ZnBi_2O_4/x$-BiOBr composite systems with $0 < x < 1$.

morphology, chemical composition, size and shape of the synthesized particles. Fig. 4 illustrates the various grain morphologies obtained by scanning electron microscopy of the composite series ($0 \leq x \leq 1$). The $ZnBi_2O_4$ sample (Fig. 4a) consists of coarse-grained agglomerations with an average size of 600 nm. As composition $x$ increases, for $x$ = 0.7, we observe in Fig. 4(b) two morphological types with two different particle contrasts characterizing a mixed system between $ZnBi_2O_4$ and BiOBr, with nanoplatelets agglomerating on the larger grains, which become increasingly uniform as we move towards $x$ = 1. This morphology is consistent with the X-ray diffraction analysis that showed the presence of these two phases. Fig. 4(c) shows a fairly uniform morphology, made up of small plate-like grains of regular size (<200 nm), attributable to the single tetragonal *P4/nmm* phase of BiOBr.

The elemental mapping and EDX spectra (Fig. S1(a–g)) confirmed the presence of Zn, Bi, O, and Br elements in the synthesized $ZnBi_2O_4$, BiOBr, and $(1 - x)ZnBi_2O_4/x$-BiOBr ($x$ = 0.1, 0.3, 0.5, 0.7, and 0.9) samples. The spatial distribution of these elements, as revealed by elemental mapping, suggests

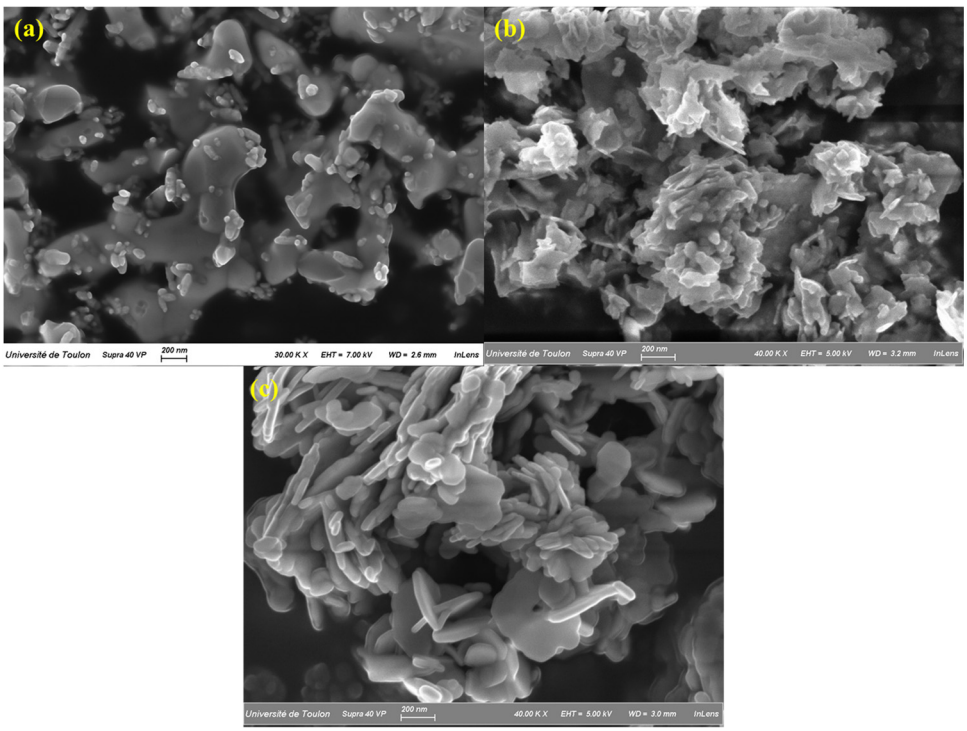


Fig. 4 SEM micrographs of $ZnBi_2O_4$ ($x$ = 0) (a) and $x$ = 0.7 (b) and BiOBr ($x$ = 1) (c).

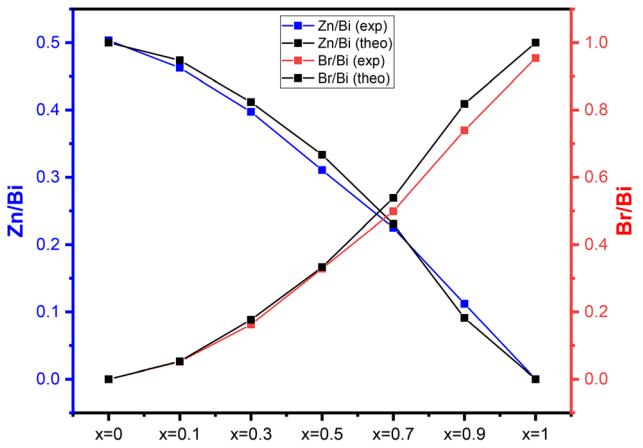


Fig. 5 Variation of the Zn/Bi and Br/Bi ratios in $(1-x)ZnBi_2O_4/x$-BiOBr composites as a function of the initial value of composition $x$.

a homogenous distribution throughout the materials. In the composites with $x = 0.7$, the elemental mapping indicates a close interface between $ZnBi_2O_4$ and BiOBr and provides evidence for the formation of heterojunctions. The presence of all four elements in the composite further confirms the successful integration of both components. Moreover, Table S1 shows the atomic percentages of the elements zinc, bromine, and bismuth in all composites. Fig. 5 shows the evolution of Zn/Bi and Br/Bi atomic ratios in $(1-x)ZnBi_2O_4/x$-BiOBr composites, obtained by EDX analysis. The relative proximity of the experimental and theoretical curves for each ratio, Zn/Bi and Br/Bi, illustrates the good correlation between initial compositions and final compositions. These results confirm the formation of $ZnBi_2O_4/x$-BiOBr composites with good correlation between initial compositions $x$ and experimental compositions.

## 8. $N_2$ adsorption–desorption analysis

Brunauer–Emmett–Teller surface analysis was carried out to determine the specific surface area and porosity of the synthesized materials. Nitrogen adsorption–desorption measurements show that all three samples $ZnBi_2O_4$, BiOBr, and $x = 0.7$ display IUPAC type IV behavior (Fig. 6(a–c)), confirming the presence of mesopores. Fig. 6(d–f) shows the pore size distributions, calculated using the Barrett–Joyner–Halenda (BJH) method from the desorption branch of the isotherms. The pure $ZnBi_2O_4$ sample (Fig. 6d) exhibits a broad distribution with a pronounced peak centered around 4–15 nm. The pure BiOBr sample (Fig. 6f) exhibits a flatter and more heterogeneous pore size distribution (10–20 nm), with no distinct peak. In comparison, the optimal composite $x = 0.7$ (Fig. 6e) shows a stronger and more distinct mesoporous structure, with a noticeable peak centered on a similar pore size of approximately $<1$ nm. The much higher intensity of the peak indicates a larger total pore volume, which corresponds to the significantly higher $S_{BET}$ calculation.

The $ZnBi_2O_4$ sample ($x = 0$) exhibited a particular surface area of 8.878 $m^2\ g^{-1}$, while the BiOBr sample ($x = 1$) had a specific surface area of 11.010 $m^2\ g^{-1}$. The $x = 0.7$ composite showed a higher specific surface area of 21.773 $m^2\ g^{-1}$. This higher surface area can provide more active sites for reactant adsorption, potentially enhancing the photocatalytic activity.

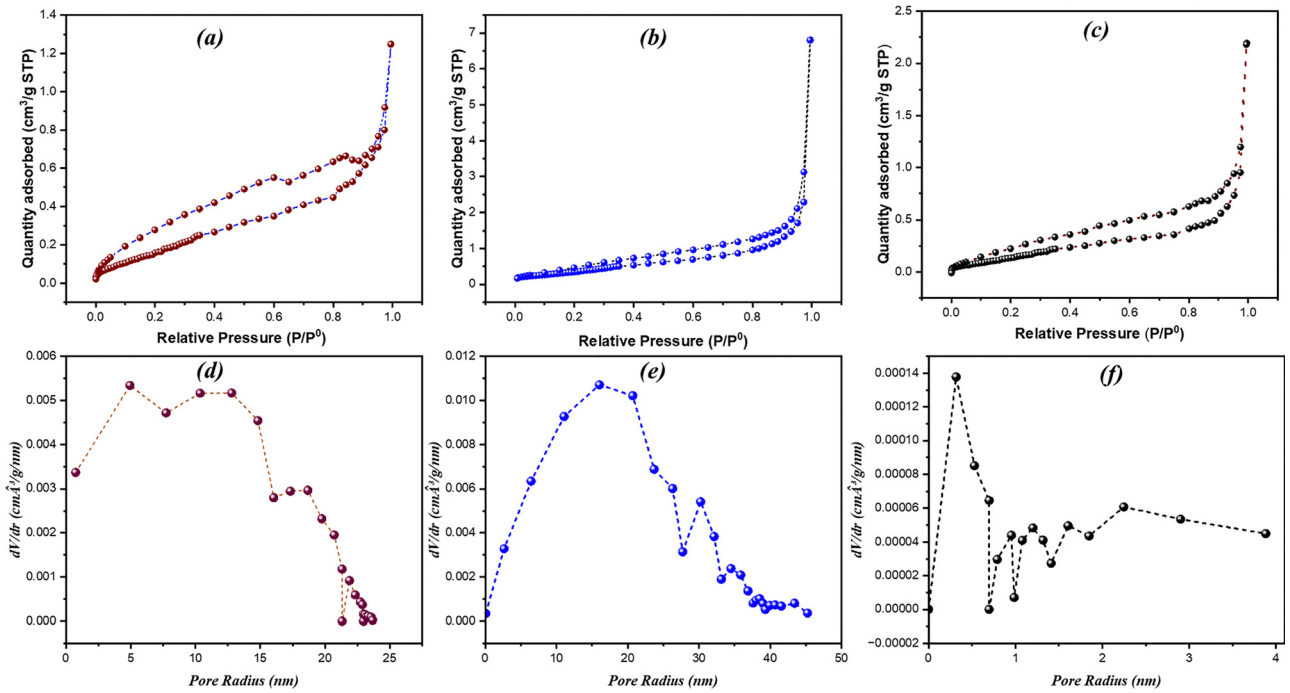


Fig. 6 $N_2$ adsorption–desorption isotherms (a)–(c) and corresponding BJH pore size distributions (d)–(f) for the $ZnBi_2O_4$ (a) and (d), $x = 0.7$ (b) and (e), and BiOBr (c) and (f) samples.

## 9. UV-visible diffuse reflectance spectroscopy

The optical properties of the synthesized photocatalysts were investigated using UV-vis diffuse reflectance spectroscopy, as shown in Fig. 7a. Sample $x = 1$ (BiOBr) exhibited a characteristic absorption edge at approximately 450 nm. In contrast, $ZnBi_2O_4$ displayed absorption edges at 440 nm and 520 nm, corresponding to its $Bi_2O_3$ and ZnO components, respectively.[21] Notably, the $(1 - x)ZnBi_2O_4/x$-BiOBr heterojunction nanocomposite showed a redshift in its absorption edge to 350 nm and maintained the 500 nm absorption, indicating that the combination of BiOBr with $ZnBi_2O_4$ extends light absorption into the visible region. The energy gap of the photocatalyst is calculated using the following formula $(\alpha h\nu)^n = A(h\nu - E_g)$, where $\alpha$, $\nu$, $h$, $E_g$, and $A$ represent the absorption coefficient, light efficiency, Planck constant, band-gap energy and proportional constant, respectively. The value of the exponent $n$ in the equation depends on the nature of the semiconductor's transition, where $n = 2$ for a direct transition and $n = 1/2$ for an indirect transition.[22] Based on the literature, $ZnBi_2O_4$ and BiOBr typically have an indirect band gap.[2,29,34] For composites, the indirect-transition model provides clean linear regions across the series, whereas direct fits are noisy and yield non-physical intercepts for several compositions (Fig. S2 and Table S2). We therefore assign an indirect optical transition as dominant for these powders.

The band-gap energy ($E_g$) of the materials can therefore be approximated by analyzing the $(\alpha h\nu)^{1/2}$ *vs.* $h\nu$ plot (Fig. 7b). The $E_g$ values for $ZnBi_2O_4$ and BiOBr were 2.84 eV and 2.95 eV, respectively. The $E_g$ values of the composites were successively: 2.96 ($x = 0.1$), 3.10 eV ($x = 0.3$), 3.12 eV ($x = 0.5$), 2.91 ($x = 0.7$), and 2.97 ($x = 0.9$). These variations, even in the case of an apparent increase in $E_g$ for some composites, can be related to the intricacies of optical absorption in a composite system with overlapping band edges, making determination of these values through the Kubelka–Munk technique difficult. Regardless, the main takeaway is that all composites, and in particular $x = 0.7$, exhibit strong absorption in the visible region, which is important for their enhanced activity. Moreover, these variations can be ascribed to the existence of structural defects and specific morphologies, including heterojunctions.

The sample with $x = 0.7$ exhibited an optimized bandgap, which is consistent with XRD, Raman, and SEM analyses. These results confirm the coexistence of both $ZnBi_2O_4$ and BiOBr phases, which enhances the surface area.

## 10. Photocatalytic activity

### 10.1. Degradation of RhB

The photocatalytic activity of the prepared samples was assessed by monitoring the degradation of Rhodamine B under visible light irradiation. The results revealed a strong dependence on BiOBr '*x*' content. Including the adsorption–desorption period of 30 min without irradiation (see Fig. 8a), the total degradation efficiency increased with increasing BiOBr content up to $x = 0.3$, reaching complete degradation (100% within 20 minutes). The observed increase of the absorption effect is due to the increasing amount of BiOBr in composites. Composites with $x = 0.5$, 0.7 and 0.9 achieved similar results in a shorter time of 10 minutes, while BiOBr alone ($x = 1$) reached 100% degradation in 25 minutes, pure $ZnBi_2O_4$ ($x = 0$) showed a much lower degradation efficiency of 25% in 25 minutes, and the composite with $x = 0.1$ reached 47% degradation in 25 minutes. This trend suggests that an optimal $ZnBi_2O_4$ : BiOBr ratio is crucial for maximizing photocatalytic performance. Reaction rate constants ($k$) were determined from the effective time $t = 0$, after the adsorption–desorption period, by fitting the $C_t/C_0$ data to a pseudo-first-order kinetic model (Fig. 8b and c). It was observed that the rate constant varied considerably as a function of the BiOBr content ($x$) in the $ZnBi_2O_4/x$-BiOBr composite (Fig. 8d). After the adsorption–desorption period of the photocatalyst, the obtained $k$ values (in $min^{-1}$, with the standard error in parentheses) were as follows:

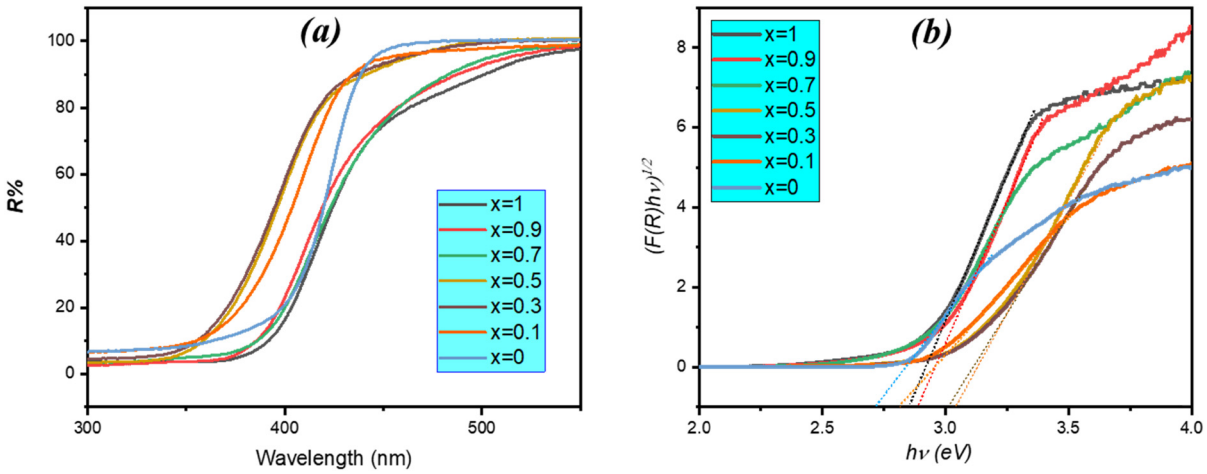


Fig. 7 (a) UV-vis reflectance spectra of different samples and (b) calculation of the $E_g$ (indirect) from plots of $(F(R)h\nu)^{1/2}$ *vs.* $h\nu$ of the prepared composites.

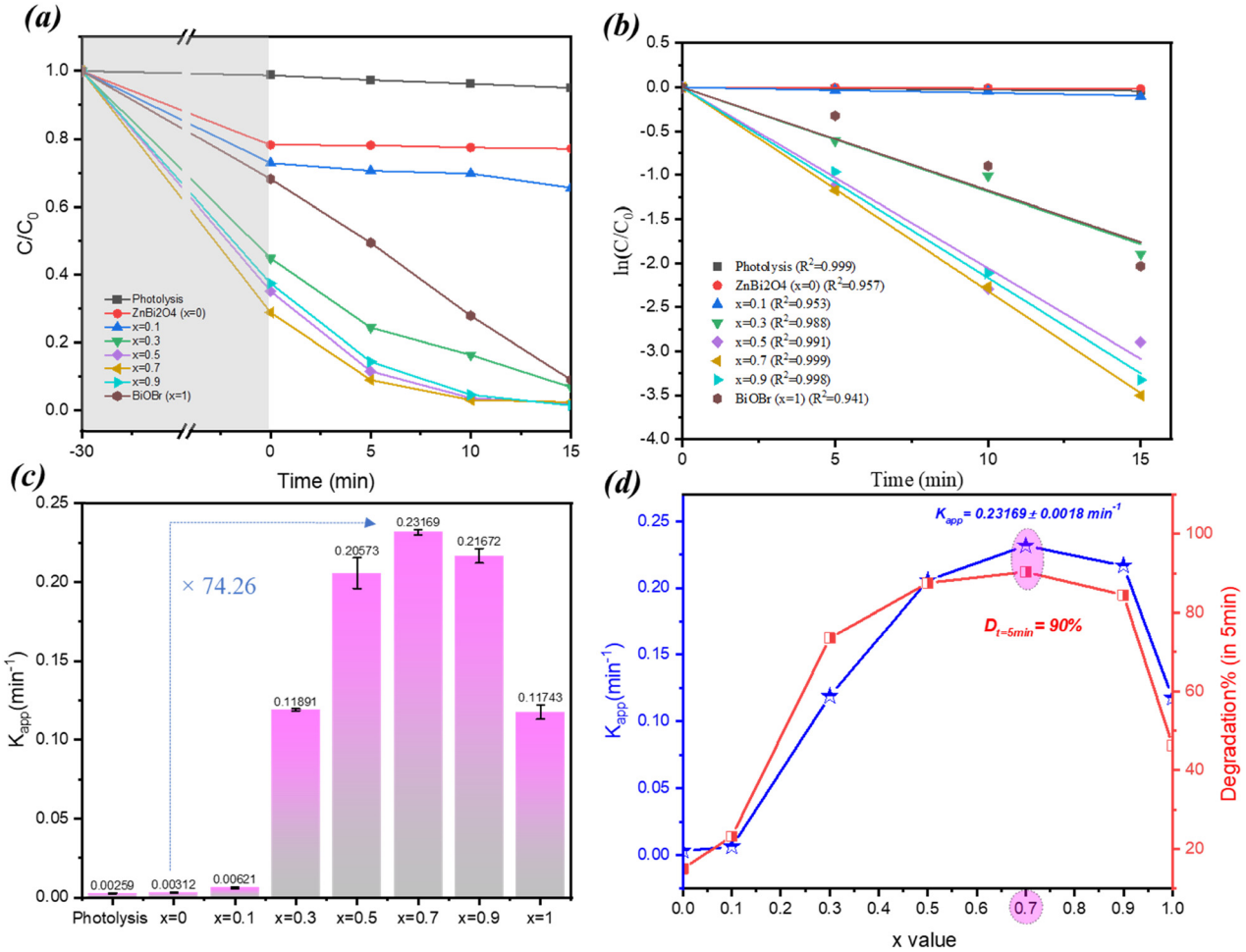


Fig. 8 Photodegradation of RhB over the $ZnBi_2O_4$/*x*-BiOBr system: (a) $C_t/C_0$ ratio *versus* time; (b) quasi-linear variations of $\ln(C_t/C_0)$ as a function of reaction time *t* (min); (c) apparent rate constants *k* ($min^{-1}$), with the pseudo-first-order reaction of RhB photocatalytic degradation; and (d) variation of degradation values and apparent rate constants over the *x* content.

$x = 0$: $k = 0.00312(\pm 3.73 \times 10^{-4})$ $min^{-1}$, $x = 0.1$: $k = 0.00621(\pm 6.8 \times 10^{-4})$ $min^{-1}$, $x = 0.3$: $k = 0.11891(\pm 6.4 \times 10^{-3})$ $min^{-1}$, $x = 0.5$: $k = 0.20573(\pm 9.7 \times 10^{-3})$ $min^{-1}$, $x = 0.7$: $k = 0.23169(\pm 1.8 \times 10^{-3})$ $min^{-1}$, $x = 0.9$: $k = 0.21672(\pm 4.6 \times 10^{-3})$ $min^{-1}$, and $x = 1$: $k = 0.11452(\pm 4.5 \times 10^{-3})$ $min^{-1}$. Moreover, the lowest rate constants were observed for $x = 0$ and $x = 0.1$. Increased photocatalytic activity was observed for the following values seen for $x = 0.3$, 0.5, and 0.7 with a maximal rate constant obtained for the composite with $x = 0.7$ (74 times higher than that of single $ZnBi_2O_4$). This indicates that the introduction of BiOBr from $x = 0.3$ to $x = 0.7$ improves reaction kinetics. For $x = 0.9$, the rate constant decreases: this could be ascribed to the morphology changes and decrease of proportion of interfaces $ZnBi_2O_4$/BiOBr.

### 10.2. Degradation of OG

Similar to the study of RhB, the photocatalytic activity of the $ZnBi_2O_4$/*x*-BiOBr composite was evaluated for the degradation of Orange G under visible light irradiation. The results showed that the composite system also exhibited notable activity in degrading this dye. Specifically, after the adsorption–desorption period (30 min), the percentage of Orange G degradation after 30 min of irradiation was 33% for pure $ZnBi_2O_4$ ($x = 0$) and 50% for pure BiOBr ($x = 1$) and reached a maximum of 100% for the composite with $x = 0.7$ (Fig. 9a and b). As in the case of RhB photodegradation, the highest value of *K* was obtained for $x = 0.7$, which is 14 times higher than the one of $ZnBi_2O_4$ (Fig. 9c). These differences in values of rate constants can be attributed to the distinct chemical properties of the two dyes, affecting their adsorption onto the photocatalyst surface and their susceptibility to oxidation/reduction by photogenerated species. Fig. 9d illustrates the evolution of the apparent rate constant ($K_{app}$) and the percentage degradation of Orange G as a function of the composition of a photocatalyst, denoted as *x*. The graph shows a direct correlation between these two parameters: the higher the rate constant, the greater the degradation rate. Maximum performance is achieved for the composition $x = 0.7$, where the photocatalyst has the highest rate constant ($K_{app} = 0.10528 \pm 0.0025$ $min^{-1}$) and ensures 100% degradation of OG in 30 minutes. Beyond this optimal value, the efficiency of the photocatalyst decreases. Comparing these results with those obtained for RhB, the composite exhibits a higher photocatalytic efficiency for the degradation

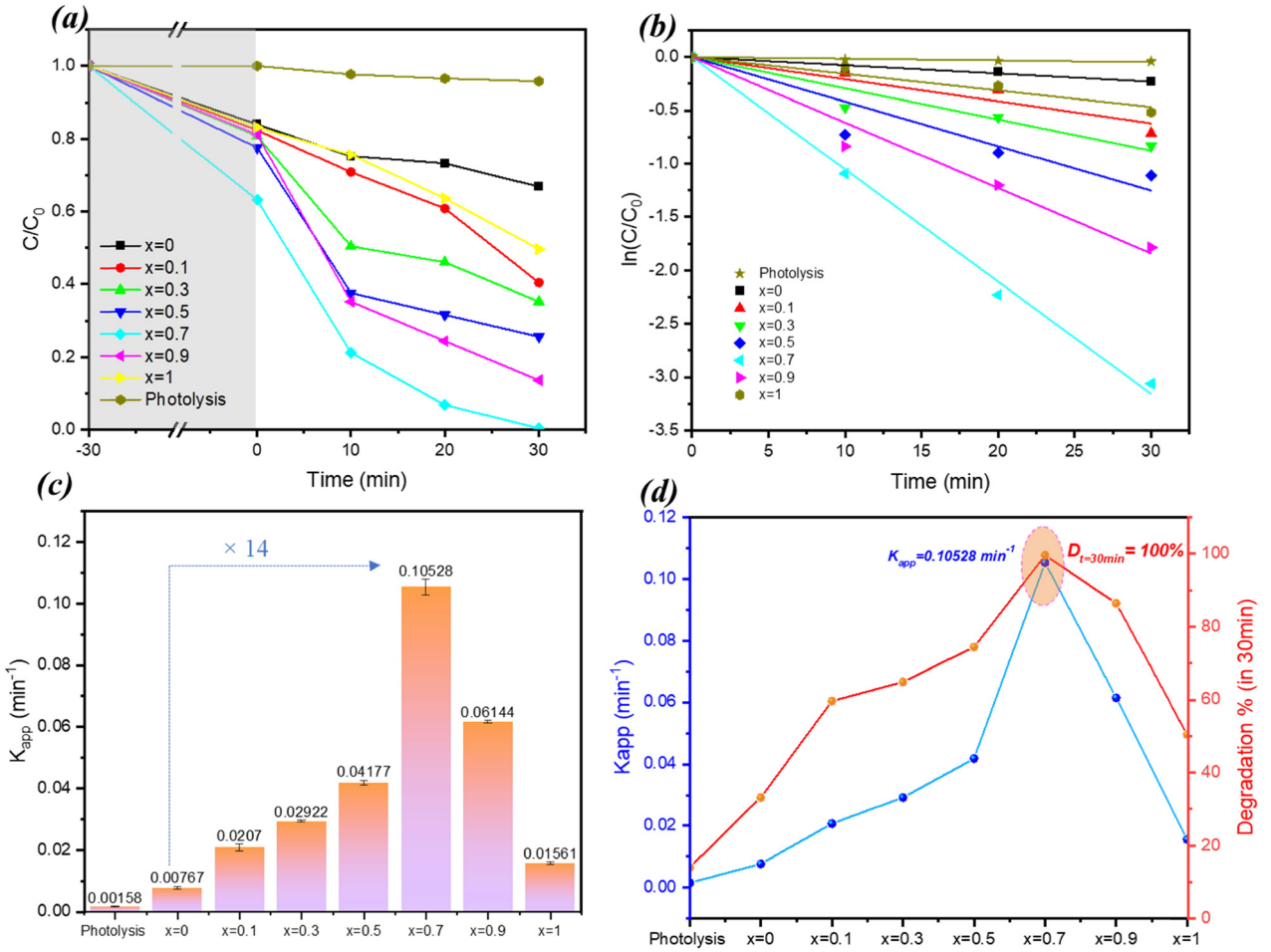


Fig. 9 (a)–(d) Photodegradation of OG over the $ZnBi_2O_4$/*x*-BiOBr system: (a) $C_t/C_0$ variation *versus* time; (b) quasi-linear variations of $\ln(C_t/C_0)$ as a function of reaction time *t* (min); (b) apparent rate constants *k* ($min^{-1}$), with the pseudo-first-order reaction of OG photocatalytic degradation; (d) variation of degradation values and apparent rate constants over the *x* content.

of RhB than for that of OG, suggesting a potential selectivity of the material according to the target pollutant.

## 11. Possible degradation mechanism

To elucidate the photocatalytic degradation mechanism, scavenging experiments were carried out by adding various radical inhibitors to the dye solution (Fig. 10). In the presence of Na2-EDTA, a hole scavenger ($h^+$), the degradation of Orange G was 18%. This suggests that holes play an important role in the degradation process. Similarly, in the presence of L-ascorbic acid, a superoxide radical scavenger ($^{\bullet}O^{2-}$), degradation was 40%, indicating the involvement of these radicals. The use of isopropanol, a hydroxyl radical $HO^{\bullet}$ scavenger, led to a degradation of 71%, suggesting a negligible involvement of hydroxyl radicals.

As reported in the literature, the conduction band edge position can be approximated using an empirical equation, as given in ref. 22, 35, and 36,

$$E_{VB} = \chi - E^0 + 0.5E_g,$$

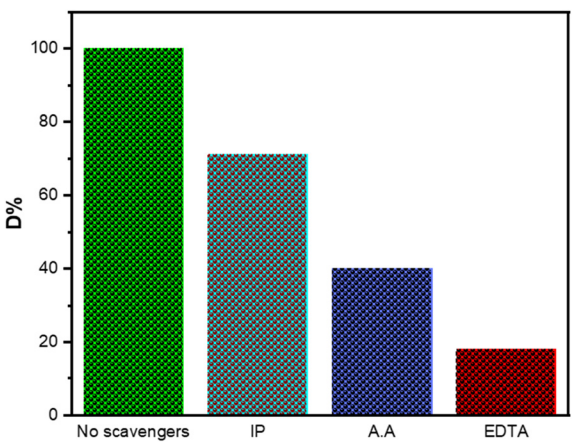


Fig. 10 Relative contributions of reactive species in the photodegradation process.

$$E_{CB} = E_{VB} - E_g,$$

where $E_{VB}$ is the valence band potential. $E_{CB}$ is the conduction band potential. $\chi$ is the electronegativity of the semiconductor.

$E^0$ is the electron energy on the hydrogen scale (4.5 eV). $E_g$ is the width of the band gap (in eV).The electronegativity of an individual atom is defined as the arithmetic mean of its electron affinity and first ionization energy. The solid electronegativity is 6.11 eV for $ZnBi_2O_4$ and 6.18 eV for BiOBr[34].[2] The calculated $E_{VB}$ and $E_{CB}$ for $ZnBi_2O_4$ are 3.03 eV, and O.19 eV, respectively. For BiOBr, the $E_{VB}$ and $E_{CB}$ are 3.15 eV and 0.205 eV.

To better understand the charge transfer process, we performed Mott–Schottky (M–S) measurements on the pure samples (Fig. 11a and b). The BiOBr graph showed a positive slope, typical of n-type semiconductor materials, and the flat band potential ($E_{fb}$) was −0.1 V (relative to Ag/AgCl). However, $ZnBi_2O_4$ showed a negative slope, indicating that it was p-type, with an $E_{fb}$ of +1.37 V *vs.* Ag/AgCl. Once converted to the normal hydrogen electrode scale (NHE) ($E_{NHE} = E_{Ag/AgCl} + 0.197$ V), the conduction band potential ($E_{CB}$) of n-type BiOBr is calculated to be +0.10 eV, and the valence band potential ($E_{VB}$) of p-type $ZnBi_2O_4$ is +1.57 eV. Experimental bandgap energies ($E_g$) from DRS data were used to obtain the respective $E_{VB}$ ($E_{VB} = E_{CB} + E_g$) for BiOBr and $E_{CB}$ ($E_{CB} = E_{VB} - E_g$) values for $ZnBi_2O_4$, which are +3.05 eV and −1.27 eV, respectively. These experimental values confirm the formation of a p–n heterojunction. The large potential difference between the bands indicates a strong driving force for charge separation, which corresponds to the observed increase in photocatalytic activity.

In order to provide quantitative evidence of the efficiency of charge transfer and the mechanistic details of photogenerated carrier separation, standard measurements of steady-state photoluminescence (PL) and time-resolved photoluminescence (TRPL) were performed. The PL spectra are shown in Fig. 11c. In general, lower PL intensity indicates a lower electron–hole recombination rate.[30] The composite sample ($x = 0.7$) shows a significant decrease in PL intensity compared to the pure samples, suggesting that the formation of the heterojunction inhibited the recombination of charge carriers. In addition, for quantitative determination of the charge carrier lifetime, TRPL decay curves were obtained (Fig. 11d). In comparison to the pure $ZnBi_2O_4$ with $\tau = 3.74$ ns ($x = 0$) and $\tau = 3.38$ ns for BiOBr ($x = 1$) samples, the optimal composite sample ($x = 0.7$) decay kinetics appear to be noticeably slower in this case. A slower decay will correlate with a longer average lifetime ($\tau = 4.36$ ns)

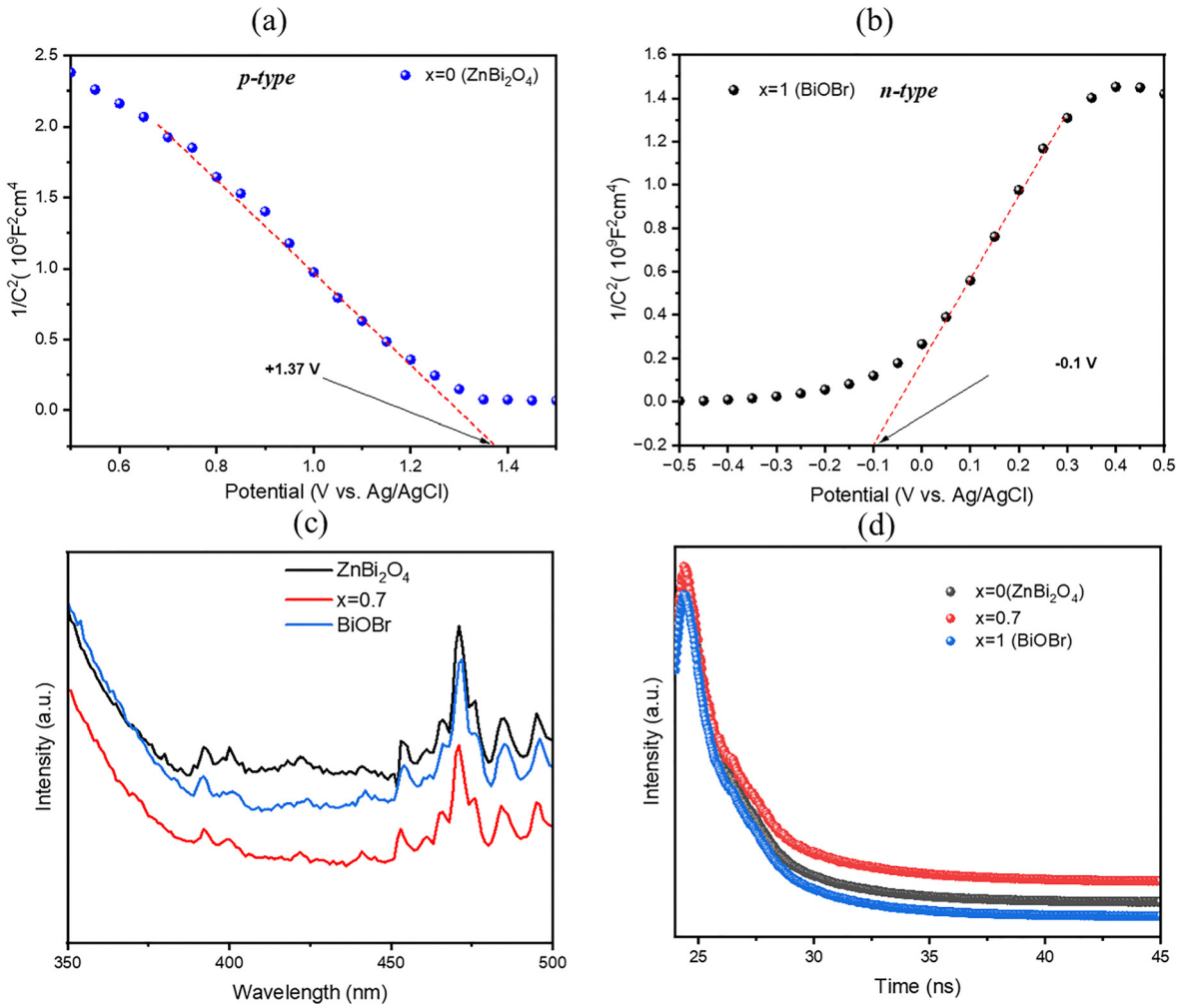


Fig. 11 Mott–Schottky plot of $ZnBi_2O_4$ (a) and BiOBr (b); photoluminescence characterization of $ZnBi_2O_4$, BiOBr, and their composites $x = 0.7$ (c) and (d).

of the charge carriers that are photo-generated. The longer lifetime is a clear indicator of spatial charge separation at the $ZnBi_2O_4$/BiOBr interface, since electrons and holes are separated to the conduction and valence bands of their respective materials (Type-II alignment) ultimately prolonging their recombination. This extended lifetime allows more charge carriers to participate in surface redox reactions, which is directly related to the improved photocatalytic performance observed for the $x$ = 0.7 composite.

Based on valence-band and conduction-band potential values determined from UV-vis measurements, an II-type heterojunction mechanism is proposed in Fig. 12. In this type of junction configuration, photo-excited electrons in the conduction band of $ZnBi_2O_4$ migrate to the conduction band of BiOBr, while photo-excited holes in the valence band of BiOBr migrate to the valence band of $ZnBi_2O_4$. This spatially separated charge transfer reduces electron–hole recombination and promotes the accumulation of electrons in the BiOBr conduction band and holes in the $ZnBi_2O_4$ valence band. These electrons and holes then react with adsorbed oxygen and water to form superoxide and hydroxyl radicals, respectively, which are responsible for dye degradation.

## 12. Photocatalyst stability and reusability

In order to evaluate the stability and practical use of the prepared photocatalysts, we studied the reusability of the optimal composite $(1-x)ZnBi_2O_4/x$-BiOBr ($x$ = 0.7) for the photocatalytic degradation of RhB under visible light irradiation. After each degradation cycle, the photocatalyst was recovered from the solution by centrifugation, thoroughly washed with ethanol and distilled water, and then dried before proceeding to the next cycle. Degradation was continued for five consecutive cycles, and the results are shown in Fig. 13a. The composite $x$ = 0.7 achieved 100% degradation in the initial cycle and displayed impressive and stable performance in subsequent cycles, with 92% degradation in the third cycle and 81% degradation efficiency even after five cycles. The slight reduction in activity is most likely due to the inevitable loss of photocatalyst powder mass during the washing and recovery stages of the cyclic tests and does not indicate deactivation of the catalyst itself. To further demonstrate the stability of the composite, characterization of the catalyst was performed after the fifth degradation cycle.

The XRD diagrams (Fig. 13b) before and after five photocatalysis cycles demonstrate that the most intense peaks of $ZnBi_2O_4$/BiOBr exhibit stable $2\theta$ values, meaning that the composite retains both its crystalline structure and phase composition. Some reflections vary in intensity and additional weak reflections appear due to a change in crystallinity, a change in the preferred orientation of the crystallites, and a minor change in the relative content of the phases, likely resulting from some photocorrosion after the photocatalytic cycle. Under light irradiation, BiOBr also has the potential to form oxygen vacancies on the surface, which impact local structures and scattering factors, adding to variations in peak intensity changes and producing new weak diffraction reflections associated with defect-rich regions.[2,37,38] Similarly, FTIR analysis (Fig. 13c) shows that the spectrum of the used catalyst is almost identical to that of the new sample, demonstrating the chemical stability of the composite. These results, combined with high reusability over five cycles and confirmed structural and chemical stability, lead to the conclusion that the $ZnBi_2O_4$/BiOBr composite is a stable and

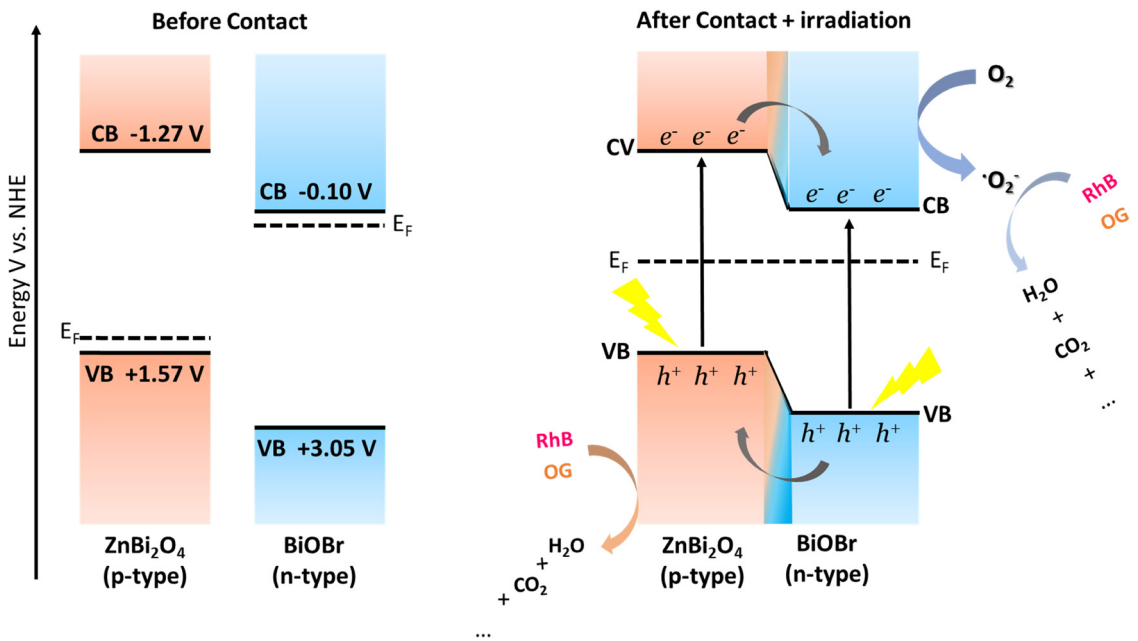


Fig. 12 Photodegradation mechanisms of RhB and OG dyes over $(1-x)ZnBi_2O_4/x$-BiOBr photocatalysts under visible light irradiation.

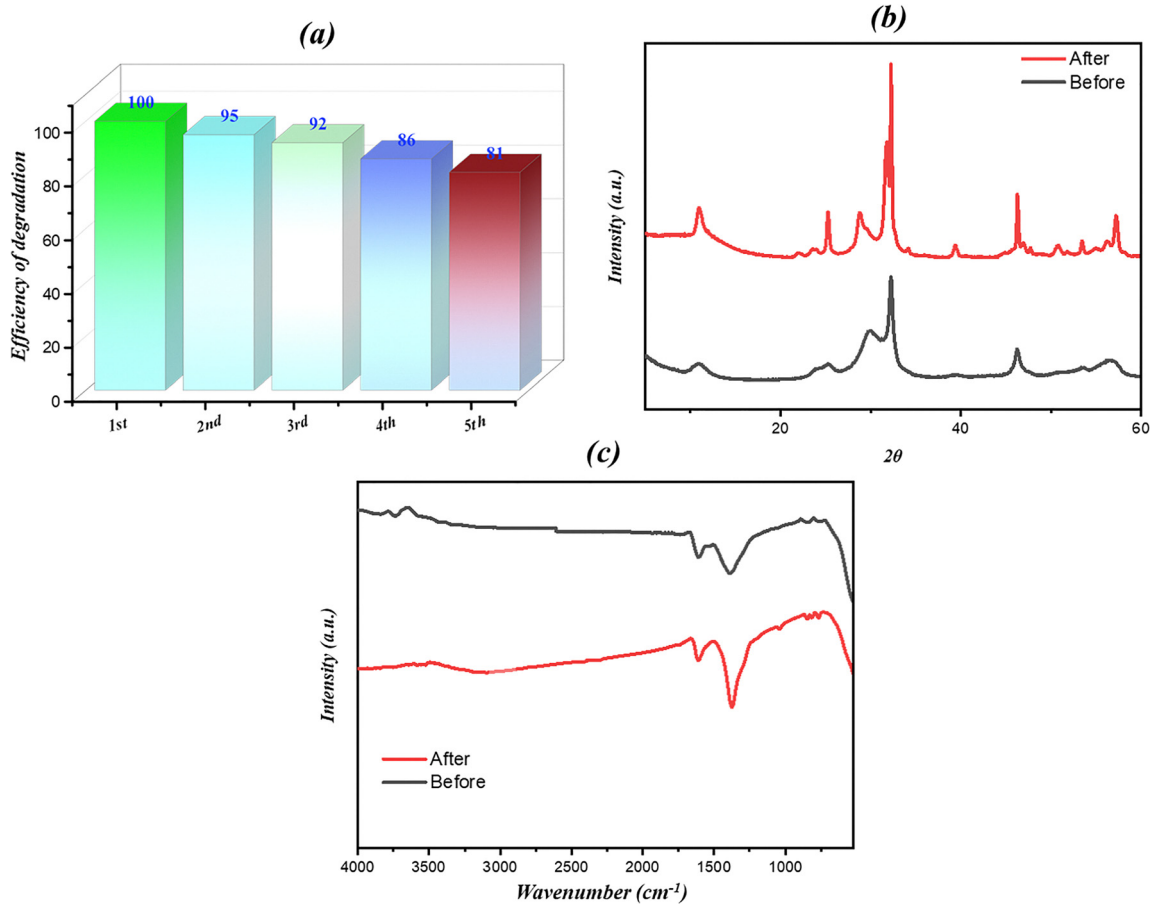


Fig. 13 (a) Photocatalytic reusability of the $x$ = 0.7 composite for RhB degradation over five consecutive cycles; (b) XRD patterns and (c) FTIR spectra of the $x$ = 0.7 composite before and after degradation cycles.

promising photocatalyst for environmental pollution control applications.

## 13. Degradation of the pharmaceutical pollutant

To confirm the intrinsic photocatalytic activity of the composite and rule out dye-sensitization effects, degradation of a colorless pollutant amoxicillin (AMX) (10 mg $L^{-1}$) was tested, using the optimal sample $x$ = 0.7. Photocatalytic degradation of AMX (10 mg $L^{-1}$) using the $x$ = 0.7 composite under visible light is shown in Fig. S3. The evolution of UV-vis absorption spectra as a function of time (Fig. S3a) demonstrates that the characteristic absorption peak of AMX around 228 nm decreased in intensity during the 150 min irradiation period, indicating that the molecular structure of the antibiotic was degraded. In Fig. S3b, the composite was tested for its degradation efficiency against this recalcitrant pollutant and demonstrated a high level of degradation efficiency, approximately 80%, within 150 min. Thus, this finding provides strong evidence for the powerful intrinsic photocatalytic activity of the $ZnBi_2O_4$/BiOBr heterojunction and is able to degrade stable pharmaceutical compounds without relying upon dye sensitization mechanisms.

## 14. Comparative evaluation and novelty

In order to evaluate the performance of the optimal composite ($x$ = 0.7) based on the existing literature, Table 2 shows the comparison of the photocatalytic activity of various recent photocatalysts based on $ZnBi_2O_4$ and BiOBr. The comparison of the results clearly highlights the performance of our material, since the apparent rate constant ($k_{app}$) for RhB degradation (0.2313 $min^{-1}$) is approximately 16 times higher than that for $ZnBi_2O_4$-graphite-based composites (0.0141 $min^{-1}$) and significantly outperforms ternary systems such as rGO–$ZnBi_2O_4$–$Bi_2S_3$ (0.0356 $min^{-1}$) and the various BiOBr composites, including BiOBr/BNQDs (0.0696 $min^{-1}$) and BiOBr/$Fe_3O_4$/RGO (0.049 $min^{-1}$). It should also be noted that this high performance is achieved by a simple two-step hydrothermal synthesis method without noble metal co-catalysts or complex multi-component structures. This demonstrates the practical value and effectiveness of the simple compositional optimization

Table 2 Comparison of the photocatalytic performance of the $ZnBi_2O_4$/BiOBr composite (this work) with that of other $ZnBi_2O_4$ and BiOBr-based photocatalysts reported in the literature

| Photocatalyst | Pollutant | Operating conditions (catalyst loading; volume; pollutant $C_0$; light source) | Irradiation source | % degradation; time | $K$ value; $min^{-1}$ | Ref. |
|---|---|---|---|---|---|---|
| $ZnBi_2O_4$/BiOBr | RhB<br>OG | 50 mg; 50 mL; 10 ppm; 250 W; $\lambda > 420$ nm | Visible | 100%; 15 min<br>100%; 30 min | 0.2313<br>0.1052 | This work |
| $ZnBi_2O_4$–graphite composites | RhB | 100 mg; 100 mL; 50 ppm; 300 W Xe lamp ($\lambda > 420$ nm) | Visible | 93.8%; 150 min | 0.0141 | 39 |
| 1.0 rGO–$ZnBi_2O_4$–2.0$Bi_2S_3$ | Indigo carmine | 100 mg; 100 mL; 50 ppm; 300 halogen lamp ($\lambda > 420$ nm) | Visible | >97%; 75 min | 0.0356 | 40 |
| $Bi_{24}O_{31}Br_{10}$ nanospheres | Cefixime (CFX) | 100 mg; 100 mL; 10 ppm; ultraviolet light UVA 24 W, 270 nm, 20 mW $cm^{-2}$ | UV | 89%; 30 min | — | 41 |
| BiOBr/BNQDs (8.3 wt% BNQDs) | RhB | 30 mg; 50 mL; 20 ppm; 300 W Xe lamp, $\lambda > 420$ nm (400 mW $cm^{-2}$) | Visible | 98.56%; 60 min | 0.0696 | 42 |
| BiOBr/GO | RhB | 1000 mg; 130 mL; 25 ppm; Düwi 25920/R7S-24 W; 81.37 W $m^{-2}$ | Visible | >99%; 120 min | — | 43 |
| $BiOBr_{0.75}I_{0.25}$ solid solution | RhB | 10 mg; 30 mL; 20 ppm; 350 W Xe lamp, $\lambda > 420$ nm | Visible | Higher RhB removal than BiOBr or BiOI; best in $BiOBr_xI_{1-x}$ series | $k_{app} \approx 3.4\times$ BiOBr (15.1× BiOI) | 44 |
| BiOBr/$Fe_3O_4$/RGO-56% | RhB | 22.5 mg; 50 mL; 20 ppm; 300 W xenon lamp with a 420 nm filter | Visible | ~96%; 60 min | 0.049 | 45 |

established in the $ZnBi_2O_4$/BiOBr system to achieve the most efficient degradation kinetics.

## 15. Conclusions

In summary, a $ZnBi_2O_4$/BiOBr composite photocatalyst was prepared using a hydrothermal method. The results show that photocatalytic performance strongly depends on the composition ratio, with the $x$ = 0.7 photocomposite exhibiting the highest activity for the degradation of RhB and OG under visible light. The improvement in performance can be attributed to the advantages of a high specific surface area (21.773 $m^2$ $g^{-1}$) and efficient charge separation resulting from a type II heterojunction. The stability tests also confirmed the reusability of the catalyst, highlighting the simplicity of composition tuning as a useful tool for producing effective Bi-based heterojunction photocatalysts for environmental remediation.

## Conflicts of interest

The authors declare that they have no known competing financial interests or personal relationships that could have appeared to influence the work reported in this paper.

## Data availability

All data supporting this study are included in the article and/or the supplementary information.

The supplementary information includes detailed experimental procedures for the synthesis of $ZnBi_2O_4$ and BiOBr, elemental composition data (EDX), atomic percentage tables, Zn/Bi and Br/Bi ratios, UV-Vis diffuse reflectance analysis, band-gap energy calculations, and photocatalytic degradation data for amoxicillin. Supplementary information (SI) is available. See DOI: https://doi.org/10.1039/d5ma00892a.

## Acknowledgements

This project was conducted at the Materials and Environment Laboratory (LME), Faculty of Science, Ibn Zohr University, Agadir, and the IM2NP Laboratory, University of Toulon, with financial support from a Cotutelle grant provided by the University of Toulon (France) and the CNRST PhD-ASsociate Scholarship – PASS national program (grant no. 32 UIZ2023, Morocco).

## References

1 S. Chaiwichian, Synthesis of novel activated carbon/$BiVO_4$ nanocomposite photocatalysts for degradation of organic compounds in wastewater, *J. Phys.: Conf. Ser.*, 2022, **2175**, 012002, DOI: 10.1088/1742-6596/2175/1/012002.

2 L. Mllaoiy, S. Bikerchalen, B. Akhsassi, O. Ouzaguine, B. Bakiz, S. Villain, A. Taoufyq, F. Guinneton, J. C. Valmalette, J. R. Gavarri and A. Benlhachemi, Engineering BiOBr nanoplatelets with {001} facet exposure: Synthesis, characterization and visible-light photocatalytic properties, *Ceram. Int.*, 2025, **51**(11), 14807–14820, DOI: 10.1016/J.CERAMINT.2025.01.323.

3 T. C. Maponya, M. J. Hato, K. D. Modibane and K. Makgopa, Metal–Organic Frameworks as Possible Candidates for Photocatalytic Degradation of Dyes in Wastewater, *Photocatal. Adv. Oxid. Process. Wastewater Treat.*, 2020, 65–91, DOI: 10.1002/9781119631422.ch3.

4 K. Qi and J. Yu, Modification of ZnO-based photocatalysts for enhanced photocatalytic activity, *Interface Sci. Technol.*, 2020, **31**, 265–284, DOI: 10.1016/B978-0-08-102890-2.00008-7.

5 B. C. B. Salgado, R. A. Cardeal and A. Valentini, Photocatalysis and Photodegradation of Pollutants, *Nanomater. Appl. Environ. Matrices*, 2019, 449–488, DOI: 10.1016/B978-0-12-814829-7.00015-X.

6 A. Bouddouch, B. Akhsassi, E. Amaterz, B. Bakiz, A. Taoufyq, S. Villain, F. Guinneton, A. El Aamrani, J. R. Gavarri and A. Benlhachemi, Photodegradation under UV Light Irradiation of Various Types and Systems of Organic Pollutants in the Presence of a Performant BiPO4 Photocatalyst, *Catalysts*, 2022, **12**(7), 691, DOI: 10.3390/catal12070691.

7 L. Yao, H. Yang, Z. Chen, M. Qiu, B. Hu and X. Wang, Bismuth oxychloride-based materials for the removal of organic pollutants in wastewater, *Chemosphere*, 2021, **273**, 128576, DOI: 10.1016/j.chemosphere.2020.128576.

8 S. Weng, B. Chen, L. Xie, Z. Zheng and P. Liu, Facile in situ synthesis of a Bi/BiOCl nanocomposite with high photocatalytic activity, *J. Mater. Chem. A*, 2013, **1**, 3068–3075, DOI: 10.1039/c2ta01004f.

9 L. Mllaoiy, S. Bikerchalen, B. Bakiz, S. Villain, A. Taoufyq, F. Guinneton, J.-R. Gavarri and A. Benlhachemi, Structure, morphological, electronic, and optical properties of Bi24O31Br10 oxybromide photocatalyst: A combined experimental study and DFT calculation, *Mater. Sci. Eng. B*, 2026, **324**, 119016, DOI: 10.1016/j.mseb.2025.119016.

10 B. Akhsassi, A. Imgharn, S. Bikerchalen, L. Mllaoiy, B. Bakiz, A. Albourine, A. Taoufyq, J.-R. Gavarri, L. Ruhlmann and A. Benlhachemi, Recent advances in BixOyClz photocatalysts for photodegradation of active pharmaceutical ingredients: A critical review, *J. Environ. Chem. Eng.*, 2025, **13**, 119077, DOI: 10.1016/j.jece.2025.119077.

11 S. Bikerchalen, L. Mllaoiy, A. Ahdour, B. Bakiz, S. Villain, A. Taoufyq, F. Guinneton, J.-C. Valmalette, J.-R. Gavarri and A. Benlhachemi, Surfactant-assisted synthesis of Bi24O31Cl10 for enhanced photocatalytic degradation of organic pollutants: Response surface methodology optimization, *Ceram. Int.*, 2025, **51**(30), 64089–64106, DOI: 10.1016/j.ceramint.2025.11.143.

12 Y. Ettahiri, A. Aziz, K. Felaous, A. Bouddouch, B. Akhsassi, L. Bouna, A. Benlhachemi and L. Pérez-Villarejo, Enhanced adsorption of Orange G dye using activated diatomite: a novel functionalization approach, *Mater. Adv.*, 2025, **6**, 5171–5183, DOI: 10.1039/D5MA00536A.

13 S. Bikerchalen, B. Akhsassi, B. Bakiz, S. Villain, A. Taoufyq, F. Guinneton, J.-R. Gavarri and A. Benlhachemi, Photocatalytic degradation of Rhodamine B dye over oxygen-rich bismuth oxychloride Bi24O31Cl10 photocatalyst under UV and Visible light irradiation: Pathways and mechanism, *J. Phys. Chem. Solids*, 2025, **196**, 112342, DOI: 10.1016/j.jpcs.2024.112342.

14 K. Fritah, M. Khachane, A. Bouddouch, B. Akhsassi, B. Bakiz, A. Taoufyq, A. El Aamrani and A. Benlhachemi, New insight for enhanced photocatalytic activity of $Bi_{4-x}La_xTi_3O_{12}$ ($0 \leq x \leq 1$) solid solution: A case study on degradation of Rhodamine B under UV light irradiation, *Opt. Mater.*, 2024, **150**, 115182, DOI: 10.1016/J.OPTMAT.2024.115182.

15 A. Ibhadon and P. Fitzpatrick, Heterogeneous Photocatalysis: Recent Advances and Applications, *Catalysts*, 2013, **3**, 189–218, DOI: 10.3390/catal3010189.

16 A. E. Gahrouei, S. Vakili, A. Zandifar and S. Pourebrahimi, From wastewater to clean water: Recent advances on the removal of metronidazole, ciprofloxacin, and sulfamethoxazole antibiotics from water through adsorption and advanced oxidation processes (AOPs), *Environ. Res.*, 2024, **252**, 119029, DOI: 10.1016/J.ENVRES.2024.119029.

17 H. Dong, G. Zeng, L. Tang, C. Fan, C. Zhang, X. He and Y. He, An overview on limitations of TiO2-based particles for photocatalytic degradation of organic pollutants and the corresponding countermeasures, *Water Res.*, 2015, **79**, 128–146, DOI: 10.1016/J.WATRES.2015.04.038.

18 X. Huang, M. Sun, W. Sun, Z. Li, H. Chen and J. Zhao, One-step hydrothermal formation of porous N-graphyne decorated $TiO_2/Ti_3C_2$ composites with enhanced photocatalytic activity, *Int. J. Hydrogen Energy*, 2024, **55**, 581–591, DOI: 10.1016/j.ijhydene.2023.11.203.

19 P. M. Kibasomba, S. Dhlamini, M. Maaza, C. P. Liu, M. M. Rashad, D. A. Rayan and B. W. Mwakikunga, Strain and grain size of TiO2 nanoparticles from TEM, Raman spectroscopy and XRD: The revisiting of the Williamson-Hall plot method, *Results Phys.*, 2018, **9**, 628–635, DOI: 10.1016/J.RINP.2018.03.008.

20 H. Kaur, A. Kumar, R. R. Koner and V. Krishnan, Metal-organic frameworks for photocatalytic degradation of pollutants, in *Nano-Materials as Photocatalysts for Degradation of Environmental Pollutants: Challenges and Possibilities*, Elsevier, 2020, pp. 91–126, DOI: 10.1016/B978-0-12-818598-8.00006-7.

21 G. Hosseinzadeh, S. Zinatloo-Ajabshir and A. Yousefi, Innovative synthesis of a novel ZnO/ZnBi2O4/graphene ternary heterojunction nanocomposite photocatalyst in the presence of tragacanth mucilage as natural surfactant, *Ceram. Int.*, 2022, **48**, 6078–6086, DOI: 10.1016/j.ceramint.2021.11.146.

22 B. Akhsassi, A. Bouddouch, Y. Naciri, Y. Ettahiri, B. Bakiz, A. Taoufyq, S. Villain, F. Guinneton, J. R. Gavarri and A. Benlhachemi, Visible light-driven type II p-Bi3O4Cl/n-BiPO4 heterojunction for effective photocatalytic photodegradation, *Ceram. Int.*, 2024, **50**, 32338–32352, DOI: 10.1016/J.CERAMINT.2024.06.041.

23 S. Wang, C. Li, Y. Qi, J. Zhang, N. Wang, M. Liu, B. Zhang, X. Cai, H. Zhang, S. Wei, G. Ma, J. Yang, S. Chen and F. Zhang, Etched BiVO4 photocatalyst with charge separation efficiency exceeding 90%, *Nat. Commun.*, 2025, **16**, 3776, DOI: 10.1038/s41467-025-59076-8.

24 D. Fang, X. Li, S. Chi, J. Dang, X. An, T. Jin and J. Wang, Construction of a novel surface plasmon resonance enhanced Z-scheme Cu|CuBi2O4/Bi/Bi2O3 photocatalyst film for effective organic pollutant degradation and simultaneous hydrogen evolution, *Mater. Sci. Semicond. Process.*, 2025, **191**, 109374, DOI: 10.1016/j.mssp.2025.109374.

25 M. S. Alkathy, V. F. Barbosa, R. P. Bonini, M. D. Teodoro, F. L. Zabotto and J. A. Eiras, Correlation of Structural Properties and Ferroelectricity in Cobalt and Iron Co-Doped Aurivillius Ceramics Based on Rietveld Refinement Analysis, *Cryst. Res. Technol.*, 2025, **60**, DOI: 10.1002/crat.202500022.

26 L. Lin, X. He, X. Zhang, W. Ma, B. Zhang, D. Wei, S. Xie, Q. Zhang, X. Yi, Y. Wang and A. Nanocomposite, of Bismuth

Clusters and $Bi_2O_2CO_3$ Sheets for Highly Efficient Electrocatalytic Reduction of CO 2 to Formate, *Angew. Chem., Int. Ed.*, 2023, **62**, e202214959, DOI: 10.1002/anie.202214959.

27 Z. Yang, C. Yang, R. Chen, Y. Zhu, L. Zhang, Y. Li and C. Li, Electron trapping fluorine stabilizing Bi–O motif for pH-universal CO2 electroreduction to formate at industrial-level current density, *J. Energy Chem.*, 2025, **110**, 263–269, DOI: 10.1016/j.jechem.2025.06.031.

28 K.-Y. Hwa, A. Santhan, C.-W. Ou and C.-H. Wang, A Zinc Oxide Interconnected Hydroxypropyl-Beta-Cyclodextrin/rGO Nanocomposite as an Electrocatalyst for Melatonin Detection: An Ultra-Sensitive Electrochemical Sensor, *Sensors*, 2025, **25**, 3266, DOI: 10.3390/s25113266.

29 B. T. Huy, P. T. Nhi, N. T. T. Vy, D. N. N. Khanh, N. T. M. Tho, N. Q. Thang, D. T. Sy, B. Q. Minh and N. T. K. Phuong, Design of novel p–n heterojunction $ZnBi_2O_4$-ZnS photocatalysts with impressive photocatalytic and antibacterial activities under visible light, *Environ. Sci. Pollut. Res.*, 2022, **29**, 84471–84486, DOI: 10.1007/s11356-022-21810-w.

30 L. Mllaoiy, S. Bikerchalen, B. Akhsassi, B. Bakiz, S. Villain, A. Taoufyq, F. Guinneton, H. Hajjoul, J.-R. Gavarri and A. Benlhachemi, In situ preparation of 3D flower like $BiOBr/Bi_{24}O_{31}Br_{10}$ composite by annealing hydrothermal method for the ciprofloxacin degradation under simulated sunlight irradiation, *Mater. Sci. Semicond. Process.*, 2026, **201**, 110060, DOI: 10.1016/j.mssp.2025.110060.

31 X. Dou, Y. Chen and H. Shi, $CuBi_2O_4$/BiOBr composites promoted PMS activation for the degradation of tetracycline: S-scheme mechanism boosted Cu2+/Cu+ cycle, *Chem. Eng. J.*, 2022, **431**, 134054, DOI: 10.1016/j.cej.2021.134054.

32 A. Rubbens, M. Drache, P. Roussel and J. P. Wignacourt, Raman scattering characterization of bismuth based mixed oxides with $Bi_2O_3$ related structures, *Mater. Res. Bull.*, 2007, **42**(9), 1683–1690, DOI: 10.1016/j.materresbull.2006.11.036.

33 C. Heterostructures, K. Zhou, F. Withers, Y. Cao, S. Hu, G. Yu and C. Casiraghi, Raman Modes of $MoS_2$ Used as Fingerprint of van der Waals Interactions, *ACS Nano*, 2014, **8**(10), 9914–9924, DOI: 10.1021/nn5042703.

34 K. Dilly Rajan, D. Srinivasan, P. P. Gotipamul, S. Khanna, S. Chidambaram and M. Rathinam, Design of a novel ZnBi2O4/Bi2O3 type-II photo-catalyst via short term hydrothermal for enhanced degradation of organic pollutants, *Mater. Sci. Eng. B*, 2022, **285**, 115929, DOI: 10.1016/j.mseb.2022.115929.

35 A. Bouddouch, B. Akhsassi, Y. Ettahiri, L. Mllaoiy, B. Bakiz, F. Guinneton, S. Villain and A. Benlhachemi, Enhanced photocatalytic activity of $BiPO_4$ towards the photo-degradation of Rhodamine B: Effect of precursor phosphates ($Na_2HPO_4$, $KH_2PO_4$, and $NH_4H_2PO_4$) on $BiPO_4$ structure, morphology and optical properties, *Next Mater.*, 2025, **9**, 100975, DOI: 10.1016/j.nxmate.2025.100975.

36 S. Bikerchalen, L. Mllaoiy, N. Saddik, B. Bakiz, S. Villain, A. Taoufyq, F. Guinneton, J.-C. Valmalette, J.-R. Gavarri and A. Benlhachemi, Optimization of solvothermal synthesis parameters for Bi24O31Cl10: Enhanced photocatalytic performance, degradation pathways, and mechanism of organic pollutants, *J. Phys. Chem. Solids*, 2026, **209**, 113267, DOI: 10.1016/j.jpcs.2025.113267.

37 X. Wang, Y. Zhao, F. Li, L. Dou, Y. Li, J. Zhao and Y. Hao, A Chelation Strategy for In-situ Constructing Surface Oxygen Vacancy on {001} Facets Exposed BiOBr Nanosheets, *Nat. Publ. Gr.*, 2016, 1–11, DOI: 10.1038/srep24918.

38 H. Li, J. Shang, Z. Ai and L. Zhang, Efficient Visible Light Nitrogen Fixation with BiOBr Nanosheets of Oxygen Vacancies on the Exposed {001} Facets, *J. Am. Chem. Soc.*, 2015, DOI: 10.1021/jacs.5b03105.

39 N. T. M. Tho, B. T. Huy, D. N. N. Khanh, H. N. N. Ha, V. Q. Huy, N. T. T. Vy, D. M. Huy, D. P. Dat and N. T. K. Phuong, Facile synthesis of $ZnBi_2O_4$-graphite composites as highly active visible-light photocatalyst for the mineralization of rhodamine B, *Korean J. Chem. Eng.*, 2018, **35**, 2442–2451, DOI: 10.1007/s11814-018-0156-z.

40 N. T. M. Tho, B. T. Huy, D. N. N. Khanh, N. T. T. Vy, N. Q. Thang, D. T. Sy, L. H. Hai and N. T. K. Phuong, Visible-Light Degradation of Organic Dye Based on a Heterostructure Photocatalyst, *Top. Catal.*, 2020, **63**, 1157–1168, DOI: 10.1007/s11244-020-01280-5.

41 O. Baaloudj, A. A. Assadi, M. Azizi, H. Kenfoud, M. Trari, A. Amrane, A. A. Assadi and N. Nasrallah, Synthesis and Characterization of $ZnBi_2O_4$ Nanoparticles: Photocatalytic Performance for Antibiotic Removal under Different Light Sources, *Appl. Sci.*, 2021, **11**, 3975, DOI: 10.3390/app11093975.

42 Y. Qin, X. Peng, T. Wu, Y. Zhong, H. Xu, Z. Mao and L. Zhang, Construction of BiOBr/BNQDs Heterostructure Photocatalyst and Performance Studies of Photocatalytic Degradation of RhB, *Catalysts*, 2025, **15**, 771, DOI: 10.3390/catal15080771.

43 E. Bárdos, V. Márta, L. Baia, M. Todea, G. Kovács, K. Baán, S. Garg, Z. Pap and K. Hernadi, Hydrothermal crystallization of bismuth oxybromide (BiOBr) in the presence of different shape controlling agents, *Appl. Surf. Sci.*, 2020, **518**, 146184, DOI: 10.1016/j.apsusc.2020.146184.

44 X. Zhang, C.-Y. Wang, L.-W. Wang, G.-X. Huang, W.-K. Wang and H.-Q. Yu, Fabrication of $BiOBrxI_{1-x}$ photocatalysts with tunable visible light catalytic activity by modulating band structures, *Sci. Rep.*, 2016, **6**, 22800, DOI: 10.1038/srep22800.

45 M. Zheng, X. Ma, J. Hu, X. Zhang, D. Li and W. Duan, Novel recyclable BiOBr/Fe 3 O 4/RGO composites with remarkable visible-light photocatalytic activity, *RSC Adv.*, 2020, **10**, 19961–19973, DOI: 10.1039/D0RA01668C.